Optics Letters

Hybrid integration of an evanescently coupled AlGaAs microdisk resonator with a silicon waveguide by nanoscale-accuracy transfer printing

B. Guilhabert,[1,*] J. McPhillimy,[1] S. May,[2] C. Klitis,[2] M. D. Dawson,[1] M. Sorel,[2] and M. J. Strain[1]

[1]Institute of Photonics, Department of Physics, University of Strathclyde, Glasgow G1 1RD, UK
[2]School of Engineering, University of Glasgow, Oakfield Avenue, Glasgow G12 8LT, UK
*Corresponding author: benoit.guilhabert@strath.ac.uk

Received 24 July 2018; revised 7 September 2018; accepted 9 September 2018; posted 10 September 2018 (Doc. ID 338393); published 3 October 2018

Hybrid integration of a III-V microdisk resonator on a silicon-on-insulator waveguide platform is demonstrated. Transfer printing with nanoscale accuracy is used to micro-assemble an evanescently coupled all-pass microdisk resonator with a targeted coupler gap of 100 nm using pre-fabricated AlGaAs and silicon components. Transmission measurements show hybrid resonances with a loaded Q-factor of 7×10^3 and a cavity finesse of over 100.

https://doi.org/10.1364/OL.43.004883

Silicon has become well established as a platform for large-scale photonic integrated circuit (PIC) design. The technology has been driven by attractive material features such as transparency at telecommunications wavelengths, a high refractive index contrast with air and oxide materials, and compatibility with electronics foundry technology facilitating deployment in high volume manufacturing. A wealth of optical devices and functions has been demonstrated on this platform, including signal routing and filtering, high-speed modulation, environmental sensing, and optical signal processing [1,2]. These functions have been realized using a relatively limited toolbox of building block devices such as single-mode waveguides, evanescent field couplers, p-i-n junctions, and wavelength selective filters. Furthermore, the native third-order nonlinearity of silicon has facilitated nonlinear optical functionality, including signal broadcasting [3] and photon pair generation [4]. Nevertheless, the silicon platform has some limitations on performance imposed by material properties. Silicon does not exhibit a second-order nonlinearity due to its centro-symmetric structure, making it unsuitable for realizing low power consumption electro-optical modulators or spontaneous downconversion photon sources. The efficiency of the third-order nonlinearity is limited by the proximity of the material bandedge to commonly used telecommunications wavelengths, inducing significant two-photon absorption and related losses. Other material platforms, including lithium niobate [5] and compound III-V semiconductors [6], have complementary properties with strong χ^2 and wide bandgaps, but do not have the maturity of silicon technologies for the realization of large-scale PIC design.

One potential solution to augment silicon PICs with additional optical functionality is to integrate these complementary materials onto the silicon platform. For example, die bonding of thin film lithium niobate onto silicon ring resonators has been achieved to allow electro-optical modulation [7]. A potentially attractive method for such hybrid integration is transfer printing (TP). This is a micro-assembly methodology where devices can be fully fabricated in their respective foundries and assembled without the need for critical post-processing stages [8]. In addition to compatibility with dense integration of hybrid devices across PICs, it allows for the integration of multiple material devices on a single chip by straightforward post-fabrication assembly. To date, the development of TP has focused on the versatility of the materials integration with notable demonstrator devices in various fields, including opto-genetic probes [9], micron-size light-emitting diodes and arrays [10,11], photodetectors [12], lasers on silicon substrates [13], and nanowire lasers integrated with polymer waveguides [14]. Recently, direct assembly of vertically coupled, single-mode silicon waveguides has been realized [15], showing the potential for the assembly of multi-material PICs requiring high accuracy device placement.

This Letter presents the direct integration of III-V material micro-resonators with pre-processed silicon waveguides using a TP technique. Evanescent coupling is achieved by printing the resonators adjacent to the silicon bus waveguide with a target separation of 100 nm.

The host chip used in this demonstration is fabricated on a standard 220 nm thick silicon-on-insulator platform. The silicon waveguides are fabricated using electron beam lithography into a hydrogen silsequioxane resist that acts as a hard mask for

the subsequent reactive ion etching. Waveguides are 500 nm wide and fully etched to the buried oxide lower cladding. The microdisk resonators are fabricated on an Al_xGa_{1-x} As platform. The top 270 nm thick core layer has a 30% aluminium content and is grown on a 0.5 μm thick AlAs undercladding layer and a GaAs substrate. Microdisks are fabricated using electron beam lithography into ZEP resist and subsequent reactive ion etching, reaching the GaAs substrate. The sample is then immersed in 5:1 buffered hydrofluoric acid to selectively etch the high aluminium content lower cladding layer. The disks are fully released from the undercladding and distributed across the exposed GaAs substrate. The microdisks are 5 μm in radius. Figure 1 shows the calculated mode field overlap of the fundamental mode of the silicon waveguide with the AlGaAs disk material as a function of the gap between the edges of the two structures. As is expected, given the exponential decay of the mode evanescent tail, the mode overlap reduces exponentially as a function of the coupling gap. Therefore, similarly to a monolithic silicon evanescent field coupler, a coupling gap in the 100 nm range is required to effectively couple to the disk. To demonstrate the hybrid integration technique, a gap of 100 nm between the AlGaAs disk and silicon waveguide was targeted.

The machine used to perform the TP process has 6 deg of freedom with stage repeatable precision down to ±25 nm over a 40 mm travel range with a minimum encoder step of 5 nm. Roll and pitch are by angular steps of $\pm 25 \times 10^{-5}$°, and the yaw angle is by 2×10^{-6}°. The stage stack is coupled to a microscope that serves to image the devices through the manipulating polydimethylsiloxane printing head (stamp). The entire system is computer controlled through a custom graphical user interface. This precise stage control allows the alignment of single-mode waveguides with a single axis accuracy of ≈100 nm [15]. Precise placement accuracy is achieved using an alignment technique with nonperiodic registration markers on the SOI and efficient pattern recognition [16]. The host silicon chip is first referenced to the TP tool translational grid by alignment to the on-chip registration marks. The AlGaAs microdisk is then picked up from the donor substrate and translated to a position close to a registration mark on the host substrate. The microdisk is held above the registration marks and translated using 50 nm steps across the marker position. The images captured at each position are then processed to produce a correlation map. The peak of the correlation in each axis registers the suspended microdisk to the machine translation grid and the host sample reference. Given the absolute registration of both the disk and the donor substrate to the TP tool translation grid, the disk can then be positioned with a target separation of its centroid to the center of the target silicon waveguide. This process is shown in schematic in Fig. 2(a). Figure 2(b) shows an scanning electron microscopy (SEM) image of a partially underetched AlGaAs microdisk on its native substrate. Once the disk has been picked up and spatially referenced, it is moved into the desired position and brought into contact with the exposed buried oxide lower cladding surface of the host substrate. It is important to note that the release of the microdisk is not mediated by any polymeric or solvent interlayer as previously reported in other demonstrations [8,10,11,14], relying instead on the intimate bonding of two atomically smooth semiconductor layers where Van der Waal bonding may be present. Optical and SEM images of a microdisk printed alongside a silicon waveguide are shown in Figs. 2(c) and 2(d), respectively.

The coupling gap achieved by the printing process was characterized using a high magnification SEM image of the coupling region. A pixel intensity profile, the dashed line in Fig. 3(a), is taken as an example of the gap measurement technique. The picture has two matching calibrations; the

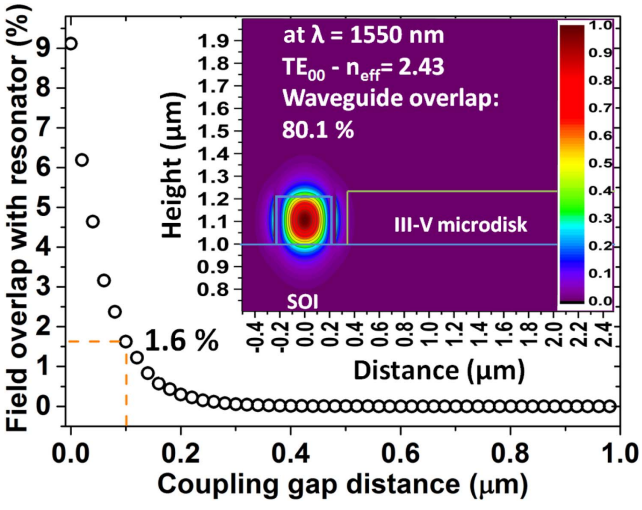

Fig. 1. Si ($n = 3.47$) ridge waveguide fundamental mode field overlap over an evanescently coupled AlGaAs microdisk ($n = 3.24$) against the coupling gap distance in air ($n = 1$) and on a silica substrate ($n = 1.45$). The dashed line indicates the mode overlap for a coupling gap of 100 nm. Inset: fundamental calculated mode for the silicon bus waveguide calculated using the refractive indices given above.

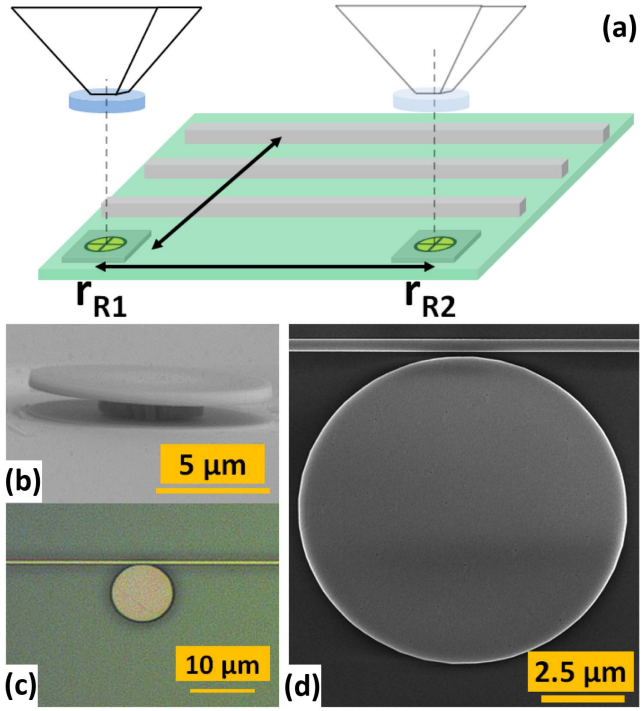

Fig. 2. Schematic of the TP alignment method to achieve a precise alignment between Si bus waveguide and microdisk resonator (a). SEM image of an AlGaAs microdisk resonator suspended on its growth substrate (b). (c) Optical micrograph and (d) SEM image of the hybrid III-V/Si all-pass filter assembled by TP.

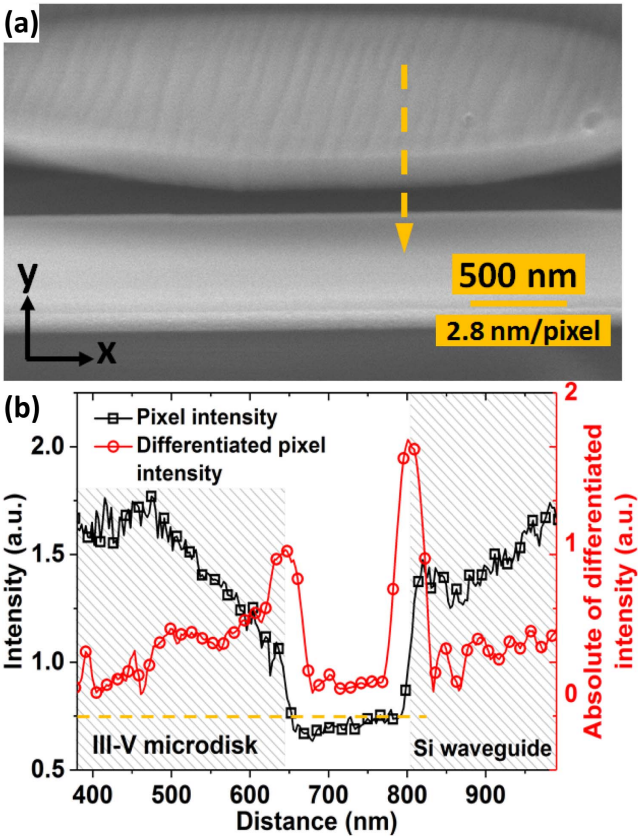

Fig. 3. (a) SEM image of the coupling gap between the AlGaAs microdisk resonator and the Si bus waveguide. The dashed arrow indicates the example profile position and direction analyzed in (b). (b) Pixel intensity profile and absolute value of the associated differentiated profile against distance.

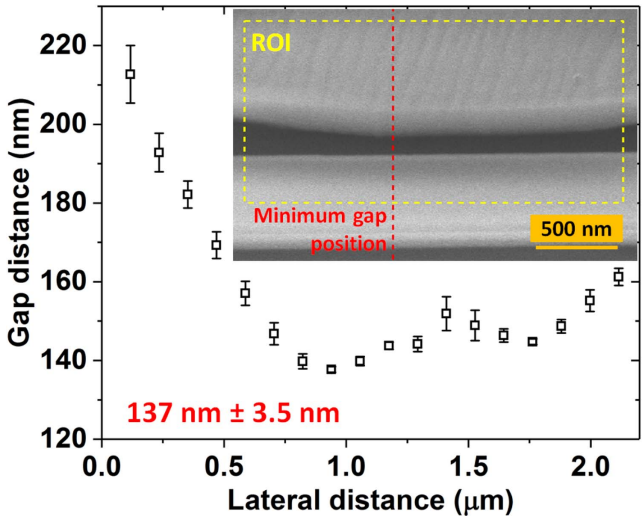

Fig. 4. Coupling gap distance statistical analysis within a ROI taken from the SEM image Fig. 3(a). Inset: ROI region and position of the minimum gap location.

SEM scale (not shown) is associated with the scale bar on the figures. This scale is corroborated by the measured width of the silicon waveguide, fabricated by electron beam lithography. Figure 3(b) shows the image intensity profile related to the line section highlighted in Fig. 3(a). Note that the length of the dashed line in Fig. 3(a) is representative only. The gap distance is computed by the differentiation of the data signal over the scan range in order to emphasise the change of slope in pixel intensity. The data points included in the gap calculation are detected as the minimum and maximum of the differentiated signal which correspond to the full width at half-maximum of the gap. Figure 3(b) shows such data used in the process. (The absolute of the differentiated signal is plotted instead for clarity.) The measurement error of the separation distance is ±2.8 nm dominated by the pixel resolution.

To measure the bus waveguide-to-resonator gap over the full coupling region, an averaging window approach is carried out across a region of interest (ROI) covering the point of closest approach. The gap is calculated for each column of pixels within this ROI, as shown in the inset of Fig. 4, and taking an average across a 40 nm lateral distance (corresponding to 5% of the total ROI width) to produce the mean and standard deviation of the computed gap values.

The recovered microdisk-to-bus waveguide separation is presented in Fig. 4 where the gap distance is plotted against the lateral distance over the ROI. It passes through a minimum of 137 nm ± 3.5 nm which represents the minimum separation between the two structures. The error takes into account the pixel resolution and the standard deviation from the statistical approach used for these results. The position of the measured minimum gap is indicated by the red vertical dashed line in the inset of Fig. 4 and is located at about 940 nm from the left-hand side of the ROI. The coupling gap analysis also shows the variation in microdisk outer rim quality where large standard deviations are attributed to fast varying gap distances, for example, from 0 nm to 500 nm of the ROI inset of Fig. 4, and around 1.5 μm, possibly indicating a localized notch defect. The recovered coupling gap at the closest approach is very close to the targeted separation of 100 nm. The variation in targeted position of the microdisk can be attributed to the systematic error within the TP machine system which possesses a minimum displacement of 5 nm per step from the optical encoders on the linear stages, a general accuracy of the system over large displacements, ±25 nm, and the linear stage jitter over time. Therefore, the results obtained are within the machine error.

The optical characterization of the hybrid structures is carried out using an injection of a TE-polarized NIR tunable CW laser from 1510 to 1640 nm with a fixed optical output power of 0.35 mW. The laser is coupled into the SOI waveguide facet through a lensed polarization maintaining single-mode optical fiber. The propagated optical signal is collected from the output facet via a microscope objective and free-space optical relay onto a calibrated photodiode.

Figure 5 shows the normalized transmission of the bus waveguide prior to and after the integration of the coupled AlGaAs microdisk cavity. Both measurements are normalized to the transmission maximum of the as-fabricated SOI waveguide alone. Excess insertion losses were measured for the wavelengths above 1550 nm after the TP process. They originate from variations in the injection optics alignment in the optical setup when comparing several consecutive alignments of the same device. Distinct resonant peaks are clearly seen in the transmission spectrum of the hybrid filter. The free spectral

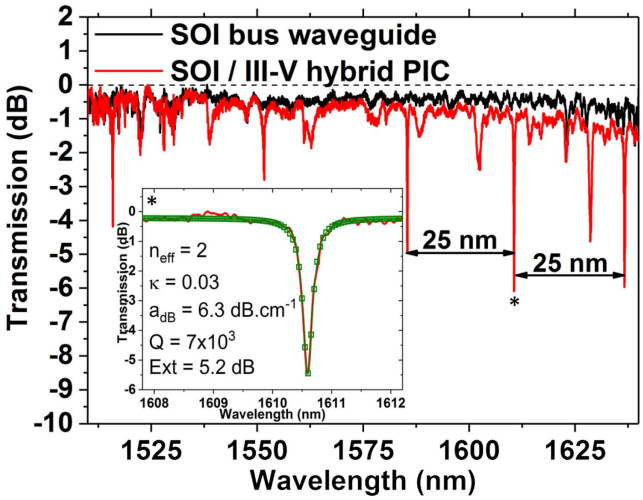

Fig. 5. Normalized optical transmission spectra of the Si bus waveguide only and the III-V/Si hybrid all-pass filter. Inset: close-up on data points and fit of a representative resonance as indicated in the full transmission. The fitted and extracted parameters are given along with the fitted data points.

range of the highest extinction, narrow linewidth resonances is ≈25 nm, corresponding to the fundamental whispering gallery mode of the microdisk resonator. These resonances are analyzed individually in terms of resonant wavelength, peak quality factor (Q), and extinction ratio. The measured data are fitted locally around the resonance to an analytical model of an all-pass filter [17]:

$$T = \frac{I_{\text{pass}}}{I_{\text{input}}} = \frac{a^2 + t^2 - 2ta\cos\varphi}{1 - 2ta\cos\varphi + (ta)^2}, \quad (1)$$

where t is the self-coupling coefficient ($t^2 = 1 - r^2$, and r the is the cross-coupling coefficient), $\phi = \beta L$ is the single-pass phase shift in the resonator (L is the round-trip cavity length, and β is the propagation constant), a is the single-pass amplitude transmission in the cavity such as $a^2 = \exp(-\phi L)$ with α ([cm^{-1}]) being the power attenuation in the cavity; a includes propagation and coupling losses. r and a are left as free parameters for the least squares error curve fitting.

The inset of Fig. 5 shows the fitted curve overlaid with the normalized measured data around 1610 nm. The fit indicates a peak wavelength at 1610.6 nm, a loaded Q factor of 7×10^3, and an extinction coefficient of 5.2 dB. The resonator power cross-coupling coefficient κ is recovered as 3%, and the distributed losses are 6.3 dB $\cdot$ cm^{-1}. These losses include both the propagation losses and the point coupling loss, giving a total round-trip loss of 0.02 dB. Two additional resonances at 1585.4 and 1636.6 nm were treated in the same way. The fits gave loaded Q factors of 9.4×10^3 and 6×10^3, respectively. Each resonance provides an extinction coefficient over 4.6 dB. Since the resonators have a small round-trip length, their finesse can be used to benchmark them against typical monolithic silicon ring resonators with radii in the few tens of microns range. A finesse of 111 was calculated at 1610.6 nm. This value compares favorably to the SOI platform with finesses of typically 100 [18] at critical coupling for racetrack resonators with a cavity length of 207.6 μm. The other selected wavelengths give finesses of 152 and 95.

In conclusion, hybrid integration of an AlGaAs microdisk resonator with a silicon photonic bus waveguide has been demonstrated using a TP technique. Cavity finesse is comparable with monolithic silicon technology, demonstrating the quality of the optical resonator after printing. The resonator was printed with positional accuracy in the tens of nanometers regime, allowing evanescent coupling of a high refractive index contrast optical waveguides. This technique demonstrates the possibility to augment silicon photonics with complementary materials using micro-assembly, for example, to allow high efficiency second- and third-order nonlinear processes on a silicon platform.

The corresponding dataset can be found at DOI: 10.15129/7200947a-69f1-4398-96e3-92b31ae50e99.

Funding. Engineering and Physical Sciences Research Council (EPSRC) (EP/P013597/1, EP/L021129/1, EP/P005624/1, EP/P013570/1).

REFERENCES

1. R. Soref, IEEE J. Sel. Top. Quantum Electron. **12**, 1678 (2006).
2. F. Morichetti, C. Ferrari, A. Canciamilla, and A. Melloni, Laser Photonics Rev. **6**, 74 (2011).
3. F. Morichetti, A. Canciamilla, C. Ferrari, A. Samarelli, M. Sorel, and A. Melloni, Nat. Commun. **2**, 296 (2011).
4. S. Azzini, D. Grassani, M. J. Strain, M. Sorel, L. G. Helt, J. E. Sipe, M. Liscidini, M. Galli, and D. Bajoni, Opt. Express **20**, 23100 (2012).
5. G. Poberaj, H. Hu, W. Sohler, and P. Günter, Laser Photonics Rev. **6**, 488 (2012).
6. D. T. Spencer, T. Drake, T. C. Briles, J. Stone, L. C. Sinclair, C. Fredrick, Q. Li, D. Westly, B. R. Ilic, A. Bluestone, N. Volet, T. Komljenovic, L. Chang, S. H. Lee, D. Y. Oh, M.-G. Suh, K. Y. Yang, M. H. P. Pfeiffer, T. J. Kippenberg, E. Norberg, L. Theogarajan, K. Vahala, N. R. Newbury, K. Srinivasan, J. E. Bowers, S. A. Diddams, and S. B. Papp, Nature **557**, 81 (2018).
7. L. Chen, Q. Xu, M. Wood, and R. Reano, Optica **1**, 112 (2014).
8. B. Corbett, R. Loi, W. Zhou, D. Liu, and Z. Ma, Prog. Quantum Electron. **52**, 1 (2017).
9. T.-I. Kim, J. G. McCall, Y. H. Jung, X. Huang, E. R. Siuda, Y. Li, J. Song, Y. M. Song, H. A. Pao, R.-H. Kim, C. Lu, S. D. Lee, I.-S. Song, G. Shin, R. Al-Hasani, S. Kim, M. P. Tan, Y. Huang, F. G. Omenetto, J. A. Rogers, and M. R. Bruchas, Science **340**, 211 (2013).
10. A. J. Trindade, B. Guilhabert, E. Y. Xie, R. Ferreira, J. J. D. McKendry, D. Zhu, N. Laurand, E. Gu, D. J. Wallis, I. M. Watson, C. J. Humphreys, and M. D. Dawson, Opt. Express **23**, 9329 (2015).
11. C. A. Bower, M. A. Meitl, B. Raymond, E. Radauscher, R. Cok, S. Bonafede, D. Gomez, T. Moore, C. Prevatte, B. Fisher, R. Rotzoll, G. A. Melnik, A. Fecioru, and A. J. Trindade, Photonics Res. **5**, A23 (2017).
12. G. Chen, J. Goyvaerts, S. Kumari, J. V. Kerrebrouck, M. Muneeb, S. Uvin, Y. Yu, and G. Roelkens, Opt. Express **26**, 6351 (2018).
13. X. Sheng, C. Robert, S. Wang, G. Pakeltis, B. Corbett, and J. A. Rogers, Laser Photonics Rev. **9**, L17 (2015).
14. D. Jevtics, A. Hurtado, B. Guilhabert, J. McPhillimy, G. Cantarella, Q. Gao, H. H. Tan, C. Jagadish, M. J. Strain, and M. D. Dawson, Nano Lett. **17**, 5990 (2017).
15. J. McPhillimy, B. Guilhabert, C. Klitis, M. D. Dawson, M. Sorel, and M. J. Strain, Opt. Express **26**, 16679 (2018).
16. E. Anderson, Microelectron. Eng. **73–74**, 74 (2004).
17. S. L. Chuang, *Physics of Photonic Devices* (Wiley, 2009).
18. M. J. Strain, C. Lacava, L. Merrigi, I. Cristiani, and M. Sorel, Opt. Lett. **40**, 1274 (2015).